Liquid Flow Patterns and Particle Settling Velocity in a Taylor-Couette Cell Using Particle Image Velocimetry and Particle Tracking Velocimetry

Andres F. Velez[1]*, Dinesh V. Kalaga[1], and Masahiro Kawaji[1]

[1]The City College of New York

Summary

Controlling the downhole pressure is an important parameter for successful and safe drilling operations. Several types of weighting agents (i.e., high-density particles), traditionally barite particles, are added to maintain the desired density of the drilling fluid (DF). The DF density is an important design parameter for preventing multiple drilling complications. These issues are caused by the settling of the dense particles, an undesired phenomenon also referred to as sagging. Therefore, there is a need to understand the settling characteristics of heavy particles in such scenarios. To this end, simultaneous measurements of liquid phase flow patterns and particle settling velocities have been conducted in a Taylor-Couette (TC) cell with a rotating inner cylinder and stationary outer cylinder separated by an annular gap of 9.0 mm. Liquid flow patterns and particle settling velocities have been measured using particle image velocimetry (PIV) and particle tracking velocimetry (PTV) techniques, respectively. Experiments have been performed by varying the rotational speed of the inner cylinder up to 200 rev/min, which is used in normal drilling operations. Spherical particles with diameters of 3.0 mm or 4.0 mm and densities between 1.2 g/cm^3 and 3.95 g/cm^3 were used. The liquid phases studied included deionized (DI) water and mineral oil, which are the basic components of a non-Newtonian DF with a shear-thinning viscosity. The DF is a mud-like emulsion of opaque appearance, which impedes the ability to observe the liquid flow field and particle settling in the TC cell. To address this issue, a solution of carboxymethyl cellulose (CMC) with a 6% weight concentration in DI water was used. This non-Newtonian solution displays shear-thinning rheological behavior and was used as a transparent alternative to the opaque DF. For water, PIV results have shown wavy vortex flow (WVF) to turbulent Taylor vortex flow (TTVF), which agrees with the flow patterns reported in the literature. For mineral oil, circular Couette flow (CCF) was observed at up to 100 rev/min and vortex formation at 200 rev/min. For CMC, no vortex formation was observed up to 200 rev/min, only CCF. The settling velocities for all particles in water matched with the particle settling velocities predicted using the Basset-Boussinesq-Oseen (BBO) equation of motion. For mineral oil and CMC, the results did not match well with the predicted settling velocities, especially for heavy particles due possibly to the radial particle migration and interactions with the outer cylinder wall.

Introduction

Drilling is the most important operation that connects us to petroleum resources. This technology is a necessary step for both petroleum exploration and production (Islam and Hossain 2021). DFs, often referred to as drilling mud from the early use of clay and water mixtures, play an important role within the drilling industry, such as cleaning the hole by removing the drill cuttings, cooling, and lubricating the drillstring, lifting cuttings to the surface, carrying information about the formations, stabilizing the wellbore, controlling formation pressure, and suspending cuttings among others.

In drilling operations, the most important parameter to manage is downhole pressure. Proper control of this pressure is crucial to avoid multiple complications like the entry of formation fluid or gas into the wellbore. To prevent such problems, it is important to use a dense DF to maintain optimal control over the pressure. To obtain the desired density and maintain sufficient hydrostatic pressure, different types of particulate weighting agents, commonly micron-sized barite particles, are added to the DF. However, if these agents settle or sag, they can lead to several problems during the drilling and completion of the well. These issues may include induced wellbore instability, mud-weight fluctuations, well-control problems, downhole mud losses, and stuck pipes. From field experience and laboratory studies, it is well known that sag potential is higher in oil-based DF compared with water-based DF, due to the reduced base emulsion density compared with the water density.

When the sedimentation of the weighting particles occurs in a non-moving mud column, it is referred to as static sag, and when sedimentation occurs in a circulating DF flow, it is known as dynamic sag (Maxey 2007; Ofei et al. 2021; Alade et al. 2023). Several experimental studies have been conducted to measure sagging in DFs. Different techniques have been used, ranging from sag tests under static and dynamic conditions to the use of laboratory-scale flow loops (Omland et al. 2007; Ofei et al. 2021; Ahmed et al. 2022). Some of the most recent studies include the characterization of sagging through light scattering measurements, hydrostatic pressure measurements, and gamma densitometry (Ofei et al. 2021).

Sag tendency under static conditions can be studied by measuring the densities of the aged DF sample at the top and bottom sections of the cell. The static sag factor can be determined from the ratio of the density at the bottom cell to the sum of the densities at the top and bottom. The sag value should be below 0.53 to avoid sagging (Omland et al. 2007; Ofei et al. 2021; Ahmed et al. 2022; Al Jaberi et al. 2023). This static testing can be performed at vertical and inclined cell orientations (Ahmed et al. 2022; Basfar et al. 2022).

Dynamic sag tendency can be characterized in both field and laboratory settings using the viscometer sag shoe test. Using a syringe, a specific volume of the DF is extracted and weighed before and after the rotational shear is applied. The dynamic sag factor is determined by calculating the difference in the specific densities of the sample before and after shear and then multiplying this difference by a sag index, which is based on hole angle, annular velocity, rotary speed, and interval length (Bern et al. 2010; Zamora 2011). A viscometer sag

*Corresponding author; email: avelezm000@citymail.cuny.edu

Copyright © 2024 Society of Petroleum Engineers

Original SPE manuscript received for review 4 May 2023. Revised manuscript received for review 23 December 2023. Paper (SPE 219459) peer approved 17 January 2024.

Downloaded from http://onepetro.org/SJ/article-pdf/doi/10.2118/219459-PA/3347625/spe-219459-pa.pdf/1 by Andres Velez on 07 February 2024

shoe test value of 0.12 g/cm^3 (Aldea et al. 2001; Basfar et al. 2018, Basfar et al. 2022; Elkatatny 2018; Ahmed et al. 2022) or less implies minimal sagging tendency and is considered a safe region, but a value above 0.19 g/cm^3 indicates the beginning of a possible sag problem (Bern et al. 2010; Elkatatny 2018; Fadl et al. 2020).

Flow loops are considered the best equipment to provide reliable data concerning simulation and sag detection (Omland et al. 2007; Zamora 2011). The results from measurements using the flow loops are used as the baseline for developing sag-stable DFs and for approval of these fluids before their application in the field (Omland et al. 2007). Nguyen et al. (2009, 2011) evaluated dynamic sag in oil-based DFs using a flow loop and a modified rotational viscometer with the addition of a sag shoe. The authors concluded that an eccentric drillpipe induces more sag compared with a concentric drillpipe. Nguyen et al. (2014) evaluated the effects of annular velocity, pipe rotation, inclination angle, and eccentricity by using a barite sag flow loop equipped with a Coriolis mass flowmeter to measure the circulating density of the fluid. The authors concluded that the axial velocity and pipe rotation contributed almost 60% and 21%, respectively, to sag prevention, and that changing the inclination angle in the range from 60° to 45° from the vertical has the least impact on sag prevention.

Ofei et al. (2021) studied barite sag in an oil-based DF before hot rolling and after hot rolling. The approach used was different from the traditional techniques used to study barite sag. One of the tests carried out using an optical stability analyzer showed that the after hot rolling fluid is more stable compared with the before hot rolling fluid. This was further confirmed by an analysis performed using the Turbiscan® Stability Index. Other characterization techniques used included gamma densitometry and hydrostatic pressure measurements, which yielded consistent results in terms of the sedimentation behavior of barite particles in DF over time.

In connection with sagging in DFs, there have been numerous studies of particle settling velocity in Newtonian and non-Newtonian fluids that have resulted in several theoretical and empirical correlations for the drag coefficient (C_D) in terms of the particle Reynolds number $\left(\mathrm{Re}_p = \frac{\rho_l u_s D}{\mu}\right)$, where ρ_l is the fluid density, u_s is the particle velocity, D is the particle diameter, and μ is the fluid viscosity. Jalaal et al. (2010) conducted a comparison of various correlations in their study and demonstrated that the drag coefficient correlation put forward by Ferreira et al. (1998) accurately represented the resistive particle force for Reynolds number within the range of 0–10^5. Nasab (2017) determined experimentally the particle settling velocity through the free fall of three different solid particles in one Newtonian fluid (water) using a high-speed video camera to record the trajectory of the spheres and the MATLAB® image processing toolbox to analyze the recorded sequences of the particle motion. The author compared the experimental results with computational fluid dynamics simulations and a numerical solution, using a drag coefficient correlation based on previous experimental data (Schiller and Naumann 1935), and concluded that the computational fluid dynamics simulations agreed more with the experimental data that had been obtained. Song et al. (2017) studied the settling behavior of spherical and nonspherical (sphere, cube, and cylinder) particles in three different Newtonian fluids, using a visualization apparatus and a high-speed camera system. The authors developed a new correlation for the drag coefficient for spherical and nonspherical particles. The formulation of this correlation accounts for both the particle's sphericity and settling orientation, aiming to incorporate their effects.

In recent studies, different correlations have also been developed. Kalman and Matana (2022) reviewed empirical correlations and experimental works relating the C_D of spheres to the Re_p and Re_p to the Archimedes number $\left(\mathrm{Ar} = \frac{\rho_l(\rho_s-\rho_l)gD^3}{\mu^2}\right)$, where ρ_s is the particle density and g is the gravitational force. In addition, experiments with various spherical particles and Newtonian fluids were conducted using a high-speed video camera, and the data were analyzed using the tracking software to develop a new correlation of C_D in terms of Re_p. Most recently, Kalman and Portnikov (2023) carried out a series of experiments involving different particles and Newtonian fluids. They observed that a straightforward exponential function adequately represented the particle velocity in relation to distance, fitting well with all the experimental data. As a result, they formulated a concise exponential equation to describe the velocity of the particles.

Shah et al. (2007) demonstrated the insufficiency of the Newtonian fluid model to correlate the data of a single spherical particle moving in power-law fluids. The authors reanalyzed the previously published data on particle settling in several non-Newtonian fluids from five different investigations. A new model to predict the settling velocity of a spherical particle moving in inelastic power-law fluid was presented. They demonstrated that the new model predicted the measured particle settling velocity data better than the models using the Newtonian drag coefficient that was commonly used by researchers. The new model would be valid for a wide range of flow behavior index (n) ranging from 0.281 to 1.0 and Re_p between 0.001 and 1,000. Zhu et al. (2022a, 2022b) studied the impact of the wall resistance effect on particle settling behavior in concentric and eccentric annuli filled with a stagnant fluid. The authors used a high-speed camera to capture the particle settling process in a transparent annulus with different gap values of δ filled with power-law fluids, but without any rotational shear. The tests were carried out with various dimensionless diameters $\left(\frac{D}{\delta}\right)$ and Re_p. In addition, the dimensionless parameter Ar (unrelated to the settling velocity) was introduced to establish a clear model for the settling velocity of spherical particles within the annulus. Malhotra and Sharma (2012) conducted an experimental study to understand and quantify the settling velocity of spherical glass particles of different diameters ranging from 1 mm to 5 mm in seven polymer-free viscoelastic fluids in unbounded and confined parallel plate scenarios. The authors demonstrated that the elasticity of the fluids could increase or decrease the settling velocity in the confined scenario by correlating the Weissenberg number $\left(\mathrm{We} = \frac{2\lambda u_s}{D}\right)$, where λ is the relaxation time of the fluid, to the wall factor (F_W), which is the ratio of the settling velocity in the confined scenario to the unbounded scenario in the same fluid. They concluded that the retardation effect of confinement on the settling velocity decreased with increasing elasticity. Additionally, the retardation effect was reduced by the increase in the shear thinning behavior, characterized by low values of the flow behavior index (n). Okensaya et al. (2020) reported on the settling velocities of different spherical particles with a diameter ranging from 0.71 mm to 4.00 mm in stagnant viscoelastic and viscoinelastic power-law-type fluids. The authors used particle image shadowgraphy to determine the particle velocities. Their comparative analysis showed that as fluid elasticity increased, both particle Reynolds number and particle settling velocity decreased in viscoelastic fluids. Building upon these observations, the authors formulated explicit models derived from the gathered data to predict the settling velocity in stagnant viscoelastic and viscoinelastic fluids.

The literature review presented above highlights the challenges in analyzing the DF using experimental approaches due to its mud-like characteristics as an invert emulsion (Growcock and Harvey 2005; Deville 2022). Visualizing the internal interactions of different components in the DF, such as barite particle sedimentation, is difficult due to its opaque nature. As an alternative approach, this work has utilized transparent model fluids with reduced complexity to study particle sedimentation in a TC cell. In the actual drilling operation, an axial flow would be superimposed on the rotational flow of DF, and consequently, the flow deviates from circular streamlines (Chandrasekhar 1981) and no longer fits the category of TC flow. Although the axial flow would affect the heavy particle sedimentation, we have not accounted for it in this work. By applying PIV and PTV techniques, the liquid flow patterns and particle sedimentation could be imaged and analyzed to quantify the settling behavior or sag of heavy particles at various rotational speeds (0–200 rev/min). The motion of individual particles of various sizes (3.0–4.0 mm) and densities (1.2–3.9 g/cm^3) in different types of fluids, including the DF

Downloaded from http://onepetro.org/SJ/article-pdf/doi/10.2118/219459-PA/3347625/spe-219459-pa.pdf/1 by Andres Velez on 07 February 2024

components (DI water and mineral oil) and a non-Newtonian CMC solution with shear-thinning viscosity like that of the DF, has been studied in this research.

In "Materials and Methods," we provide a detailed description of the transparent model fluids used in this study and their properties compared with the DF. We also explain the PIV and PTV techniques used for imaging and analyzing liquid flow patterns and particle sedimentation. Additionally, we present an overview of the TC cell and the solid particles used. In "Results and Discussion," we present the flow patterns observed in the fluids and particle sedimentation data obtained in the TC cell. The main results are then summarized in "Conclusions."

Materials and Methods

Reference DF. The reference DF is an opaque oil-based DF, classified as a nonaqueous invert emulsion with a water-in-oil emulsion ratio of 20:80 and a density of 1.43 g/cm^3. It was synthesized in our laboratory by blending nine components provided by MI-Swaco, Schlumberger in Norway. It exhibited a non-Newtonian shear-thinning rheological behavior, which was reported by Ofei et al. (2021).

Model System. The fluids used in the present experiments were DI water and mineral oil, which are Newtonian fluids with constant viscosities, and an aqueous CMC solution, which is a non-Newtonian, shear-thinning fluid. Several samples of the CMC solutions with different concentrations of 3%, 4%, 5%, and 6% by weight were synthesized and characterized using rotational rheometry. **Table 1** summarizes the properties of the fluids used in this experimental work. Compared with water, the viscosity of mineral oil was 10 times greater and the CMC 6% solution was about 270–330 times greater under the experimental conditions used.

Fluid	Density (g/cm^3)	Viscosity (Pa·s)	Kinematic Viscosity (m^2/s)
DI water	0.998	0.001	1.0
Mineral oil	0.870	0.017	19.5
CMC 6% solution	1.001	0.278-0.337	277.7-336.6

Table 1—Fluid properties.

Spherical Particles. The test particles were spheres of different materials, sizes, and densities: polymethyl methacrylate (PMMA), cellulose acetate (CA), glass, and alumina. The particle diameter (D) was either 3.0 mm or 4.0 mm, and the particle density is listed in **Table 2.**

Material	Particle Diameter (mm)	Density (g/cm^3)
PMMA	3.0	1.2
CA	3.0, 4.0	1.3
Glass	3.0	2.5
Alumina	3.0	3.9

Table 2—Spherical particle properties.

Rheological Characterization. The rheological properties of the reference DF and CMC solution were measured using an ARES-G2 rheometer with a concentric cylinder geometry conforming to the standards sey by the Deutsches Institut für Normung (DIN). To obtain flow curves, we subjected the samples to shearing for 300 seconds at a range of shear rates up to 1,000 s^{-1} and held them at a constant temperature of either 25°C or 30°C. Although the CMC solution exhibited shear-thinning behavior, it did not possess a yield stress, unlike the oil-based DF. The yield stress would affect the particle sedimentation behavior, but the shear rates used in the present experiments were high enough such that the yield stress would not be relevant.

TC Cell Setup. The TC cell consisted of two concentric cylinders enclosed within an optical acrylic correction box. The purpose of the box was to reduce optical distortion caused by the curvature of the acrylic test section. The fixed outer cylinder had a radius of 28.0 mm (r_o), while the inner cylinder, a metallic shaft with a radius of 19.0 mm (r_i), was rotated using a direct-current (DC) motor. The resulting annular gap between the two cylinders was 9.0 mm ($\delta = r_o$-r_i). Both the correction box and outer cylinder were transparent, allowing for clear optical access and flow visualization. **Fig. 1** provides a depiction of the setup used in the laboratory.

PIV and PTV. PIV and PTV are well-established techniques to study liquid and particle motions in transparent fluids. The two methods were used to determine the velocity from the displacement of particles in a moving fluid during a prescribed time interval. PIV analyzes the displacement of a small group of seed particles between two successive images and calculates the velocity vectors in the interrogation region. The results are averaged over the interrogation region to obtain the mean velocity. On the other hand, PTV tracks the trajectories of large particles individually and calculates the instantaneous velocity from the distance traveled and elapsed time (Dracos 1996). PIV has a higher temporal resolution and provides a snapshot of the flow field, whereas PTV requires a longer time interval to track individual particles over larger distances.

Figs. 2 and 3 illustrate the experimental setup used in this study, involving a TC cell and the components for PIV and PTV measurements. **Table 3** provides a summary of the experimental conditions. A laser with a wavelength of 532 nm was used to generate a fan-shaped

Downloaded from http://onepetro.org/SJ/article-pdf/doi/10.2118/219459-PA/3347625/spe-219459-pa.pdf/1 by Andres Velez on 07 February 2024

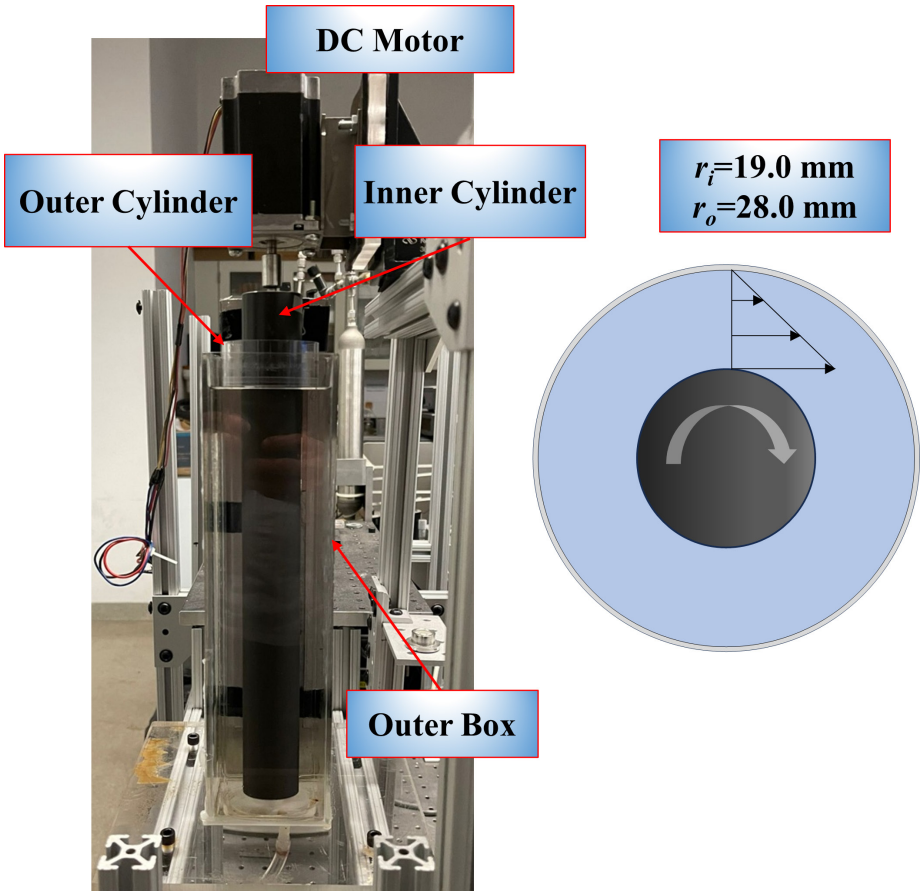

Fig. 1—Layout of the TC cell setup.

thin light sheet of approximately 2-mm thickness by passing the laser beam through a cylindrical lens. The lens was adjusted to center the laser sheet through a metallic plate with a slit, allowing for visualization of the TC cell's front plane. Hollow glass spheres with a specific gravity of 0.95 and a diameter of approximately 10 μm were used as seeding particles for PIV measurements to capture the liquid flow field in this plane. The inner cylindrical rod was rotated at speeds ranging from 0 to 200 rev/min, while a high-speed camera positioned perpendicular to the laser sheet recorded the illuminated particles. To process the obtained images, two different image analysis programs were utilized. DaVis 8.2.1, which performs image preprocessing and cross-correlation procedures to determine the instantaneous velocity field from consecutive pairs of seed particle images, was used for PIV characterization. Image J, which allows for manual tracking of individual particles and obtaining their positions and vertical and horizontal velocities, was used for PTV characterization.

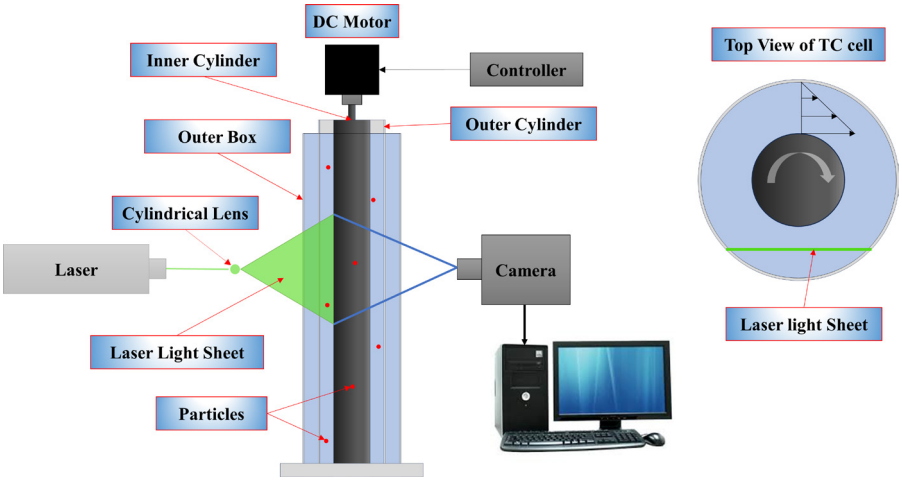

Fig. 2—Schematic for the PIV and PTV test facility.

Downloaded from http://onepetro.org/SJ/article-pdf/doi/10.2118/219459-PA/3347625/spe-219459-pa.pdf/1 by Andres Velez on 07 February 2024

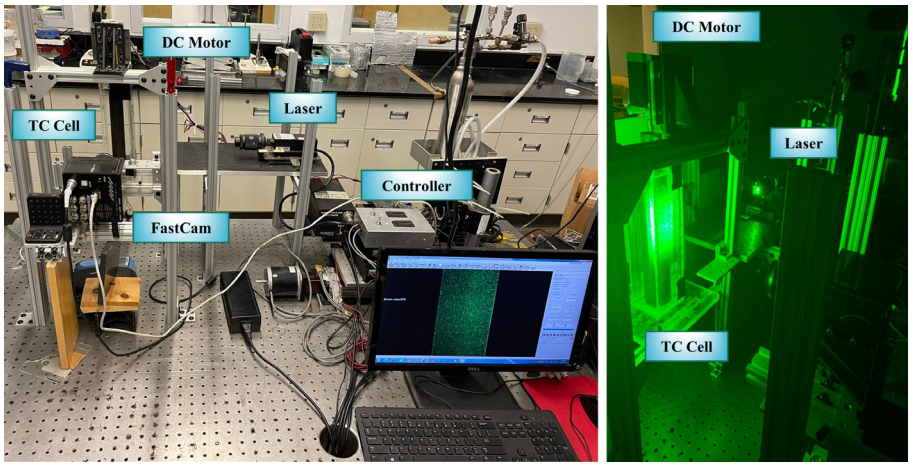

Fig. 3—Layout of PIV and PTV experimental setup.

Experimental Conditions	
Inner cylinder radius (mm)	19.0
Outer cylinder radius (mm)	28.0
Rotational speed (rev/min)	25, 100, 200
Angular velocity (rad/s)	2.6, 10.5, 20.9
Frame rate for PIV (fps)	5,000
Frame rate for PTV (fps)	2,000
Shutter speed (seconds)	1/8,000
Frame size (pixels)	1,280 × 800

Table 3—Experimental conditions for PIV and PTV techniques.

TC Flow Regime. Various flow patterns can occur in a TC cell depending on the rotational speed of the inner rod. **Fig. 4** shows the different flow transitions according to the fluid Reynolds number (Re_l), calculated using Eq. 1:

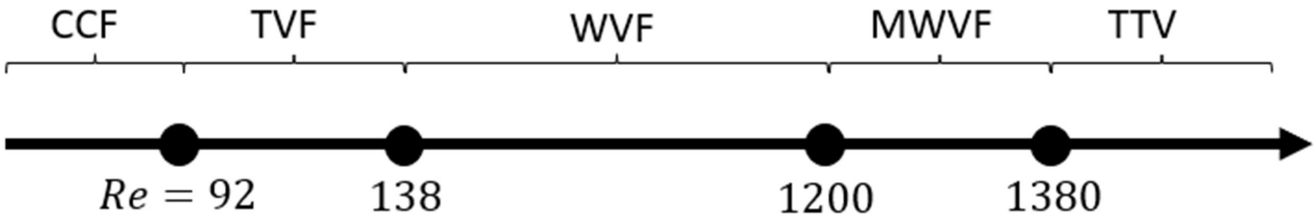

Fig. 4—Flow regime in a single-phase TC flow (Yoshida et al. 2009).

$$\mathrm{Re}_l = \frac{r_i \omega \left(r_o - r_i\right)}{\nu}, \tag{1}$$

where ν is the kinematic viscosity of the fluid and ω is the angular velocity.

The five flow patterns observed by Yoshida et al. (2009) depicted in **Fig. 4** are CCF ($\mathrm{Re}_l < 92$), Taylor vortex flow (TVF; $92 < \mathrm{Re}_l < 138$), WVF ($138 < \mathrm{Re}_l < 1{,}020$), modulated wavy vortex flow (MWVF; $1{,}020 < \mathrm{Re}_l < 1{,}380$), and TTVF ($1{,}380 < \mathrm{Re}_l <$ TTVF).

Taylor number is a dimensionless parameter that describes the relative importance of inertial to viscous forces in a fluid flow. There is a critical value, known as the Taylor critical value, that is used to determine the onset of turbulence in a fluid flow, and it represents a threshold value of the Taylor number above which a laminar flow becomes unstable and transitions to a turbulent flow. This value is approximately 1,700 and it is calculated using Eq. 2 (White 2016):

$$\mathrm{Ta} = \frac{r_i \omega^2 \left(r_o - r_i\right)^3}{\nu^2}. \tag{2}$$

Downloaded from http://onepetro.org/SJ/article-pdf/doi/10.2118/219459-PA/3347625/spe-219459-pa.pdf/1 by Andres Velez on 07 February 2024

Table 4 summarizes the corresponding Reynolds and Taylor numbers for the fluids as well as the predicted flow pattern within the TC cell.

	Rotational Speed (rev/min)		
	25	100	200
Fluid	Reynolds Number (Predicted Flow), Taylor Number		
DI water	450 (WVF), 0.096×10^6	1,800 (TTVF), 1.5×10^6	3,600 (TTVF), 6.1×10^6
Mineral oil	40 (CCF), 0.076×10^4	160 (WVF), 1.2×10^4	315 (WVF), 4.7×10^4
CMC 6% solution	1 (CCF), 0.93	5 (CCF), 13.8	11 (CCF), 54.2

Table 4—Predicted flow for the three rotational speeds evaluated in the TC cell.

Theoretical Prediction of Particle Sedimentation. In particle dynamics, the BBO equation, based on Newton's second law of motion, states that the rate of change in the particle's momentum is equal to the sum of the forces acting on the particle, such as gravitational and buoyancy forces, drag force, added mass, and minor forces like Basset history force. The BBO equation for low Reynolds number ($\mathrm{Re}_p \leq 0.2$) is written as follows:

$$\frac{1}{6}\pi D^3\rho_s\frac{du_s}{dt} = 3\pi\mu D\left(u_l-u_s\right) - \frac{1}{6}\pi D^3\nabla p + \frac{1}{12}\pi D^3\rho_l\frac{d}{dt}\left(u_l-u_s\right) + \frac{3}{2}D^2\sqrt{\pi\rho_l\mu}\int_0^t\frac{1}{\sqrt{t-\tau}}\frac{d}{d\tau}\left(u_l-u_s\right)d\tau + \frac{1}{6}\rho_s\pi D^3 g - \frac{1}{6}\rho_l\pi D^3 g + \sum_k F_k, \quad (3)$$

where D is the particle diameter, ρ_s is the particle density, ρ_l is the liquid density, μ is the fluid dynamic viscosity, u_s is the settling particle velocity, u_l is the liquid velocity, ∇p is the pressure gradient, τ is the kernel time, t is the time, g is the gravitational acceleration, and F_k represents other forces. The terms on the right-hand side of Eq. 3 correspond to viscous drag force, pressure gradient, added mass, Basset or history force, gravity force, buoyancy force, and other forces, respectively.

Consider the 1D accelerated motion of a small, rigid, spherical, particle of diameter D, falling vertically in an infinite stagnant, incompressible Newtonian fluid. In this scenario, the fluid has no vertical movement, and no other particles are in motion within it, eliminating particle-particle interactions. The fluid flow field is also large, so the particle motion is not affected by the wall effect. The mass of the spherical particles is calculated as follows:

$$m = \frac{1}{6}\rho_s\pi D^3. \quad (4)$$

The pressure gradient term can be neglected because it is only important if a large liquid pressure gradient exists and if the particle density is smaller than the liquid density (Nasab 2017). If the particle density is greater than the liquid density, Basset history force can be neglected (Jalaal et al. 2010; Torabi and Yaghoobi 2011; Malvandi et al. 2014; Fakour et al. 2018). The simplified BBO equation of motion can be written as follows:

$$m\frac{du_s}{dt} = mg\left(1-\frac{\rho_l}{\rho_s}\right) - \frac{1}{8}\pi D^2\rho_l C_D u_s^2 - \frac{1}{12}\pi D^3\rho_l\frac{du_s}{dt}, \quad (5)$$

where C_D is the drag coefficient. The terms on the right-hand side of Eq. 5 correspond to the buoyancy force, drag force, and added mass. For purposes of comparison, two different correlations for the drag coefficient were used. These drag coefficients are applicable to Newtonian fluids; therefore, they are used in the calculation of the particle settling velocity in DI water and mineral oil. The first drag coefficient correlation (C_{D1}) has a good agreement with experimental data for the particle Reynolds number (Re_p) ranging from 0 to 10^5 (Ferreira et al. 1998; Jalaal et al. 2010; Fakour et al. 2018). The second correlation (C_{D2}) agrees with data for $0 \leq \mathrm{Re}_p \leq 2\times10^3$ (Polezhaev and Chircov 2011).

$$C_{D1} = \frac{24}{\mathrm{Re}_p}\left(1+\frac{1}{48}\mathrm{Re}_p\right), \quad (6)$$

$$C_{D2} = \frac{21.12}{\mathrm{Re}_p} + \frac{6.3}{\sqrt{\mathrm{Re}_p}} + 0.25, \quad (7)$$

where

$$\mathrm{Re}_p = \frac{\rho_l u_s D}{\mu}. \quad (8)$$

With C_{D1}, the equation of motion can be rewritten as Eq. 9:

$$a\frac{du}{dt} + bu + cu^2 - d = 0, \quad (9)$$

where

$$a = \frac{1}{12}\pi D^3\left(2\rho_s+\rho_l\right), \quad (10)$$

Downloaded from http://onepetro.org/SJ/article-pdf/doi/10.2118/219459-PA/3347625/spe-219459-pa.pdf/1 by Andres Velez on 07 February 2024

$$b = 3\pi D\mu, \tag{11}$$

$$c = \frac{1}{16}\pi D^2 \rho_l, \tag{12}$$

$$d = \frac{1}{6}\pi D^3 g\left(\rho_s - \rho_l\right), \tag{13}$$

$$u = \frac{dy}{dt}. \tag{14}$$

Substituting Eq. 14 into Eq. 9, we can get the vertical trajectory equation for C_{D1} in the form of:

$$a\frac{d^2y}{dt^2} + b\frac{dy}{dt} + c\left(\frac{dy}{dt}\right)^2 - d = 0. \tag{15}$$

With C_{D2}, the equation of motion can be rewritten as Eq. 16:

$$a\frac{du}{dt} + bu + cu^{\frac{3}{2}} + du^2 - e = 0, \tag{16}$$

where

$$a = \frac{1}{12}\pi D^3\left(2\rho_s + \rho_l\right), \tag{17}$$

$$b = \frac{21.12}{8}\pi D\mu, \tag{18}$$

$$c = \frac{6.3}{8}\pi D^{\frac{3}{2}}\sqrt{\rho_l \mu}, \tag{19}$$

$$d = \frac{0.25}{8}\pi D^2 \rho_l, \tag{20}$$

$$e = \frac{1}{6}\pi D^3 g\left(\rho_s - \rho_l\right). \tag{21}$$

Substituting Eq. 14 into Eq. 16, we can obtain the vertical trajectory equation for C_{D2} in the form of

$$a\frac{d^2y}{dt^2} + b\frac{dy}{dt} + c\left(\frac{dy}{dt}\right)^{\frac{3}{2}} + d\left(\frac{dy}{dt}\right)^2 - e = 0. \tag{22}$$

Eqs. 9 and 16 are used to determine the particles settling velocity as a function of time, while Eqs. 15 and 22 are used to determine the vertical position of the particles as a function of time during their settlement in the fluid. These equations are nonlinear ordinary differential equations with known initial conditions of $u\left(0\right) = 0$ and $y\left(0\right) = 0$, which can be resolved analytically. To obtain more accurate results, MATLAB® was used.

For the case of the non-Newtonian fluid, the CMC solution follows the model of a power-law fluid, for which the shear stress is given by

$$\tau = K\left(\gamma\right)^n, \tag{23}$$

where τ and γ are the shear stress and shear rate, respectively. The n and K represent the flow behavior index and the consistency index of the power-law fluid. To obtain the flow and consistency index we must linearize Eq. 23 in the following form:

$$\log\left(\tau\right) = n\log\left(\gamma\right) + \log\left(K\right). \tag{24}$$

From plotting the results of Eq. 24, we can obtain the slope $\left(n\right)$ and the intercept in the form of $\log\left(K\right)$ from where we obtain K by solving $10^{\log K}$.

Using the model developed by Shah et al. (2007), we have the following equation:

$$\sqrt{C_D^{2-n}\mathrm{Re}_p^2} = A\left(\mathrm{Re}_p\right)^B, \tag{25}$$

where

$$A = 6.1948n^2 - 24.838n + 22.642, \tag{26}$$

$$B = -0.5067n^2 + 1.3234n - 0.1744, \tag{27}$$

and by definition, C_D and Re_p for the power-law fluid are given as (Shah et al. 2007):

Downloaded from http://onepetro.org/SJ/article-pdf/doi/10.2118/219459-PA/3347625/spe-219459-pa.pdf/1 by Andres Velez on 07 February 2024

$$C_D = \frac{4}{3}\left(\frac{Dg}{u_s^2}\right)\left(\frac{\rho_s - \rho_l}{\rho_l}\right), \tag{28}$$

$$\mathrm{Re}_p = \left(\frac{D^n u_s^{2-n}\rho_l}{2^{n-1}K}\right). \tag{29}$$

Therefore, by substituting Eqs. 28 and 29 into Eq. 25, we have the following equation:

$$\sqrt{C_D^{2-n}\mathrm{Re}_p^2} = \sqrt{\frac{4}{3}\left[\frac{g^{2-n}}{2^{2(n-1)}}\right]\left[\frac{D^{n+2}\rho_l^n\left(\rho_s - \rho_l\right)^{2-n}}{K^2}\right]}. \tag{30}$$

By rearranging Eq. 25 and substituting the solutions of Eqs. 26, 27, and 30, we can obtain the result for Re_p:

$$\mathrm{Re}_p = \frac{\left(\sqrt{C_D^{2-n}\mathrm{Re}_p^2}\right)^{\frac{1}{B}}}{A}. \tag{31}$$

By rearranging Eq. 29 and substituting the result of Eq. 31, we can obtain the theoretical terminal velocity of a particle in a power-law fluid as follows:

$$u_s = \left(\frac{2^{n-1}K\mathrm{Re}_p}{D^n\rho_l}\right)^{\frac{1}{2-n}}. \tag{32}$$

Results and Discussion

Rheological Results. Fig. 5 shows the viscosity profiles of different CMC solutions. All concentrations showed a shear-thinning rheological behavior, meaning that the viscosity decreased with increasing shear rate with the highest viscosity obtained for the CMC solution with a 6% weight concentration. For this experimental study, it was decided to work with the 6% CMC weight concentration for the PIV and PTV measurements.

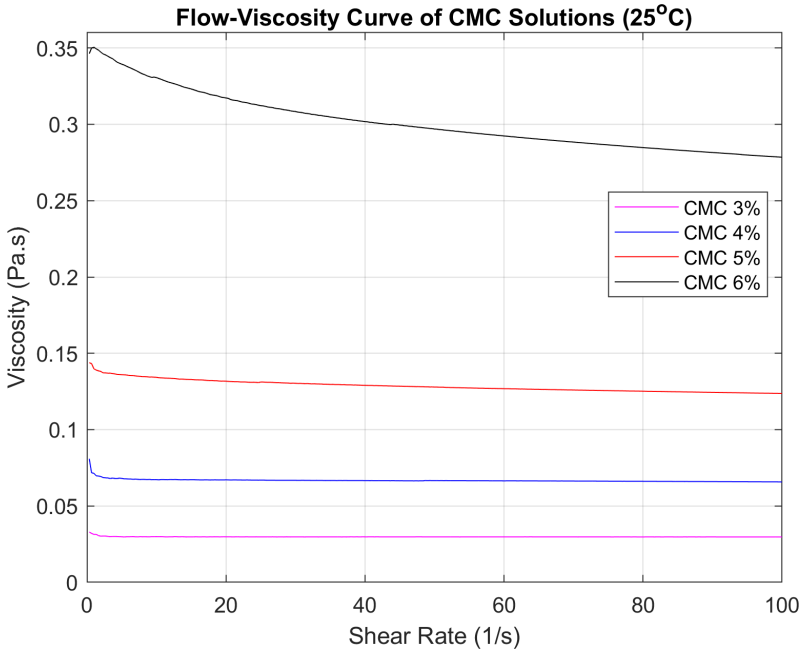

Fig. 5—Viscosity profiles for different CMC concentrations.

Fig. 6 shows comparisons of the shear stress and viscosity vs. shear rate data between the reference DF previously prepared and tested by Ofei et al. (2021), the CMC solution with a 6% weight concentration, and the mineral oil. The fluids were tested using PIV at three different rotational speeds (25, 100, and 200 rev/min), which are converted to s^{-1} units and marked as vertical dotted lines on the graph. At 25 rev/min, the DF viscosity was approximately 3.8 times higher than that of the CMC solution. At 100 rev/min, the DF viscosity was about 1.40 times higher than that of the CMC solution. Finally, at 200 rev/min, the CMC solution was approximately 1.08 times higher than that of the DF. From the rheological measurements of the CMC 6% solution, the values of n and K were determined to be 0.865 and 0.4477 Pa·s, respectively. It is noted that if Taylor vortices occur within the TC cell, then the actual viscosity of the fluid under rotational shear may be different from those obtained in the rheometer, as shown in **Fig. 6**.

PIV Measurements. PIV images of water were obtained at three different rotational speeds, and both horizontal and vertical velocity components were extracted as shown in **Figs. 7 and 8**, respectively. Cell formation can be seen in **Fig. 7a** at 25 rev/min, with clear

Downloaded from http://onepetro.org/SJ/article-pdf/doi/10.2118/219459-PA/3347625/spe-219459-pa.pdf/1 by Andres Velez on 07 February 2024

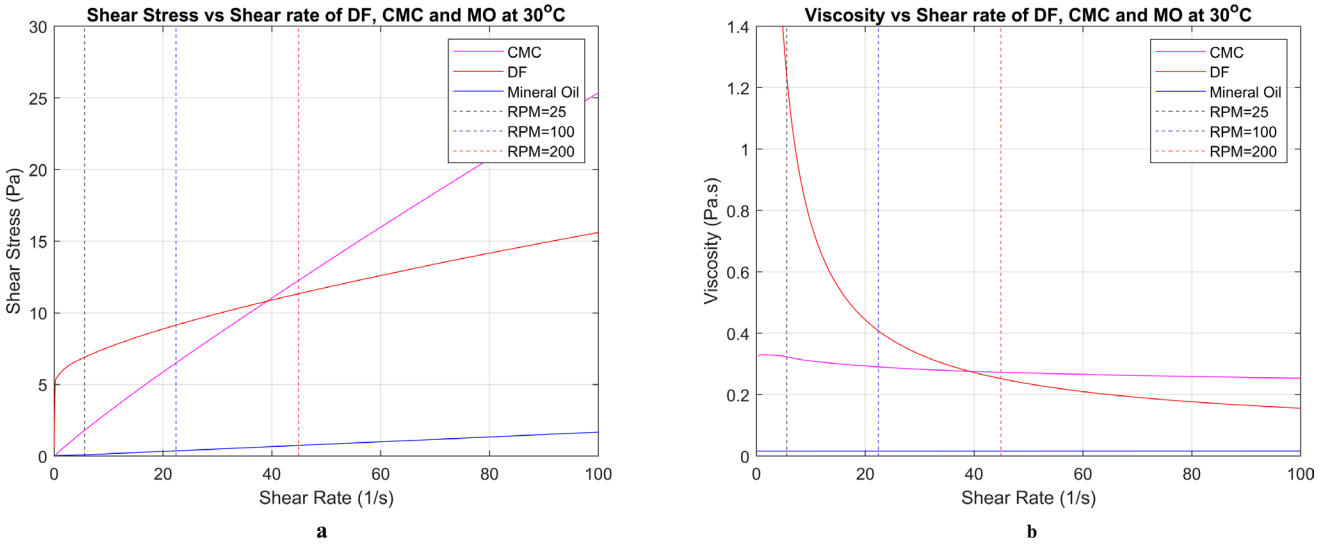

Fig. 6—Flow curves of the reference DF, CMC 6% solution, and mineral oil (MO): (a) shear stress and (b) viscosity.

boundaries but less symmetry compared with the formation observed at 100 rev/min and 200 rev/min in **Figs. 7b and 7c**, respectively. The observed flow patterns match the predicted flow patterns at all rotational speeds. Specifically, WVF was observed at 25 rev/min, corresponding to a Reynolds number of 450. At 100 rev/min and 200 rev/min, TTVF was observed, corresponding to Reynolds numbers of 1,800 and 3,600, respectively.

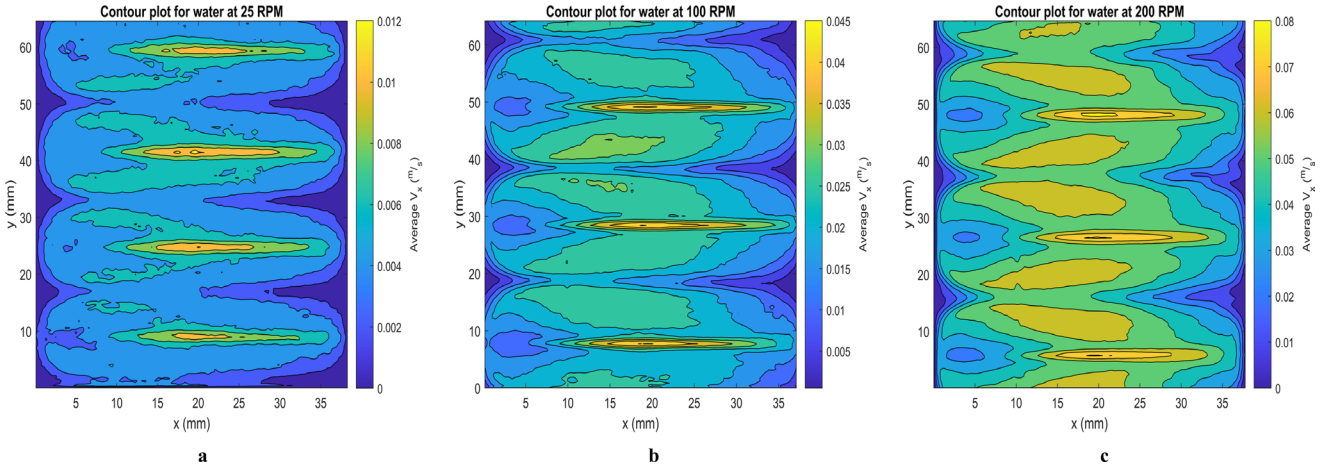

Fig. 7—Horizontal velocity fields and flow patterns for water at different rotational speeds: (a) 25 rev/min, (b) 100 rev/min, and (c) 200 rev/min.

Downloaded from http://onepetro.org/SJ/article-pdf/doi/10.2118/219459-PA/3347625/spe-219459-pa.pdf/1 by Andres Velez on 07 February 2024

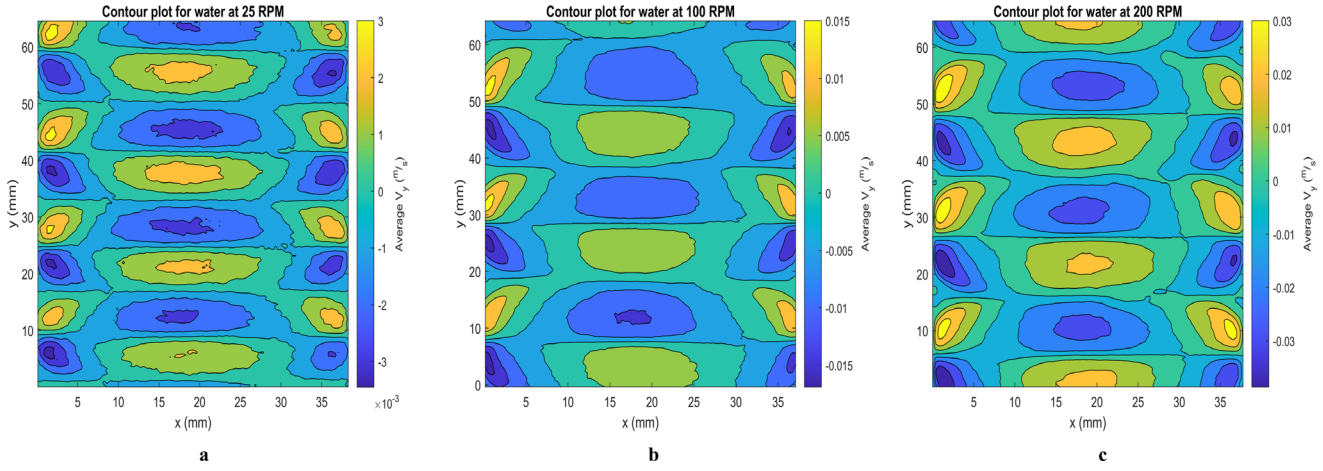

Fig. 8—Vertical velocity fields and flow patterns for water at different rotational speeds: (a) 25 rev/min; (b) 100 rev/min; (c) 200 rev/min.

Fig. 8 shows the vertical velocity fields for all rotational speeds. In each cell, the *y*-velocity component exhibited a range of negative to positive velocities, providing clear evidence of the formation of Taylor vortices in water.

Next, the horizontal and vertical velocity fields for mineral oil are shown in **Figs. 9 and 10**, respectively, for the three rotational speeds. While **Figs. 9a and 9b** do not show any evidence of cell formation, resulting in a CCF pattern, **Fig. 9c** displays cell formation, although less clearly than in water **(Fig. 7c)**. Interestingly, the predicted flow pattern for $Re_l = 160$, which corresponds to 100 rev/min, is a WVF. However, the obtained results show a CCF flow pattern, as seen in **Fig. 9b**.

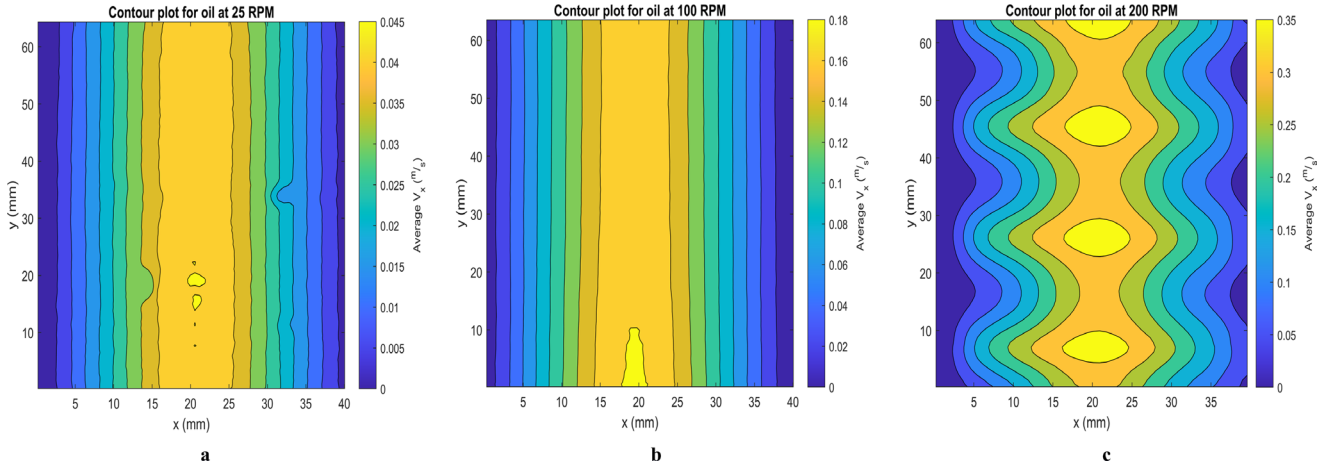

Fig. 9—Horizontal velocity fields and flow patterns for mineral oil at different rotational speeds: (a) 25 rev/min; (b) 100 rev/min; (c) 200 rev/min.

Downloaded from http://onepetro.org/SJ/article-pdf/doi/10.2118/219459-PA/3347625/spe-219459-pa.pdf/1 by Andres Velez on 07 February 2024

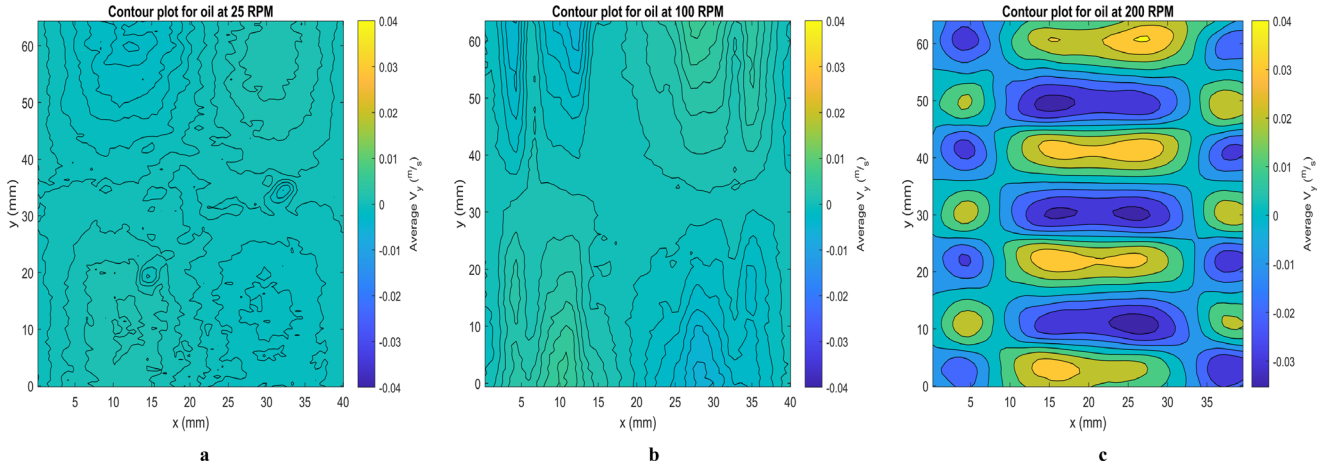

Fig. 10—Vertical velocity fields and flow patterns for mineral oil at different rotational speeds: (a) 25 rev/min; (b) 100 rev/min; (c) 200 rev/min.

The vertical velocity fields shown in **Figs. 10a and 10b** also indicate no vortex formation for rotational speeds of 25 rev/min and 100 rev/min, respectively. However, at 200 rev/min, the presence of Taylor vortices becomes apparent. Notably, the magnitudes of the vertical velocity are considerably lower than those of the horizontal velocity.

The horizontal and vertical velocity fields for the CMC solution are shown in **Figs. 11 and 12**, respectively. The flow pattern observed across all rotational speeds, corresponding to Reynolds numbers of Re_l = 1, 5, and 11, was CCF, which agreed with the predicted flow pattern.

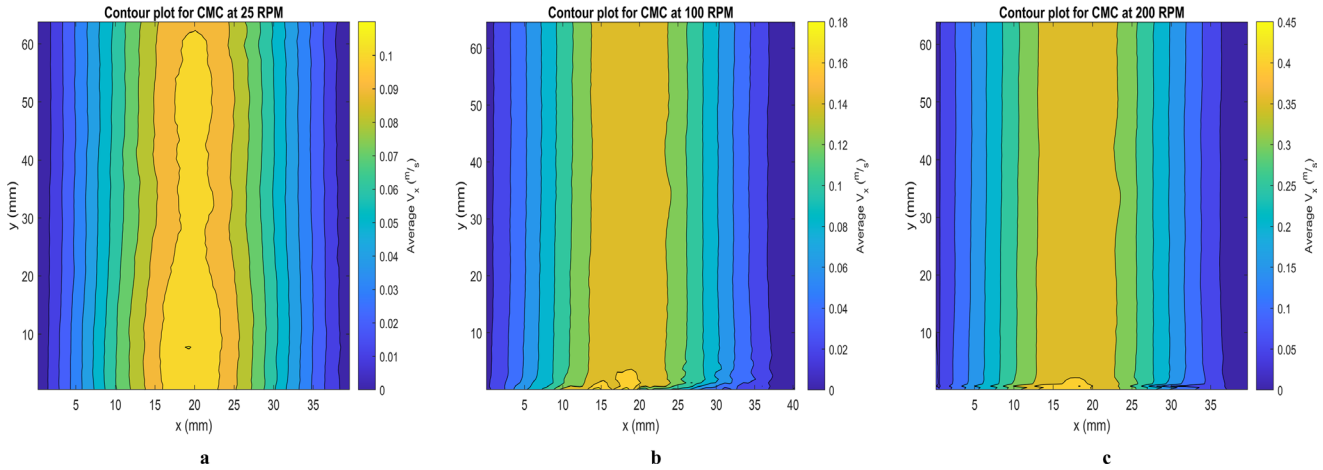

Fig. 11—Horizontal velocity fields and flow patterns for CMC 6% solution at different rotational speeds: (a) 25 rev/min; (b) 100 rev/min; (c) 200 rev/min.

Downloaded from http://onepetro.org/SJ/article-pdf/doi/10.2118/219459-PA/3347625/spe-219459-pa.pdf/1 by Andres Velez on 07 February 2024

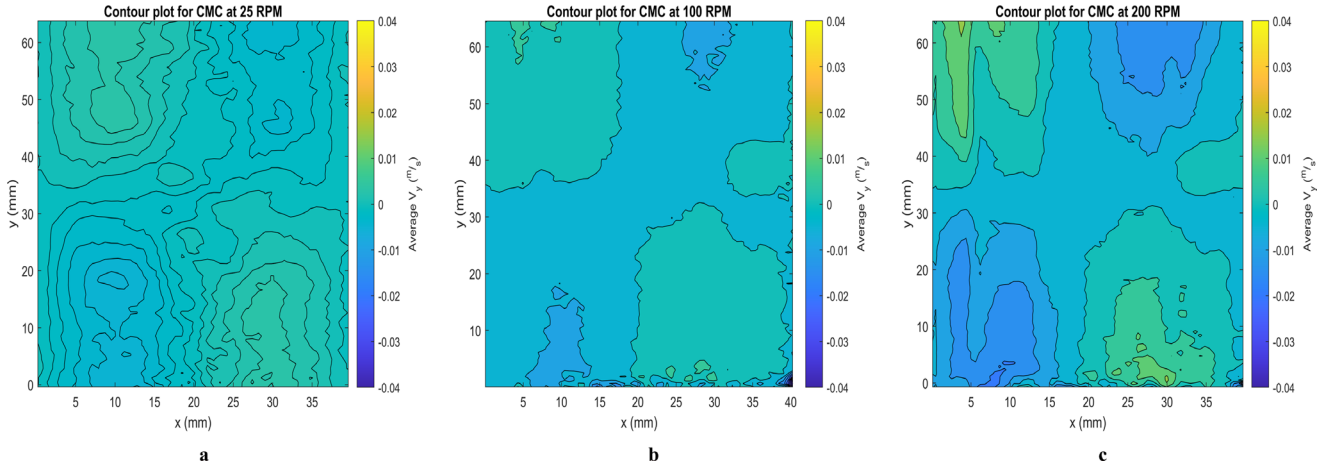

Fig. 12—Vertical velocity fields and flow patterns for CMC 6% solution at different rotational speeds: (a) 25 rev/min; (b) 100 rev/min; (c) 200 rev/min.

PTV Measurements

Effects of Rotational Speed and Particle Density on Vertical Settling Velocity. Figs. 13 through 15 show the particle velocity data obtained from PTV measurements in water, mineral oil, and CMC solution, respectively. Each data point represents the average velocity data obtained from about 100 particles. In water, the settling velocity decreased slightly as the rotational speed increased from 0 to 200 rev/min. The heavier particles (D = 3.0 mm and ρ_s = 2.5 g/cm^3 and 3.9 g/cm^3) decreased their settling velocities by up to 10% as the rotational speed increased from 25 rev/min to 200 rev/min, as shown in **Fig. 13a**. The results for the mineral oil showed larger decreases of up to 20% in the settling velocity for the heaviest particle **(Fig. 14a)**. For the CMC solution, the particle settling velocities were much lower than in water and mineral oil due to one or two orders of magnitude higher viscosity of the CMC solution. The particle settling velocity data showed mixed variations with the rotational speed, as shown in **Fig. 15a**. For the heavy particles (D = 3.0 mm and ρ_s = 2.5 g/cm^3 and 3.9 g/cm^3), the settling velocity decreased as the rotational speed increased from 25 rev/min to 100 rev/min, but the settling velocities of all the particles increased sharply as the rotational speed increased from 100 rev/min to 200 rev/min.

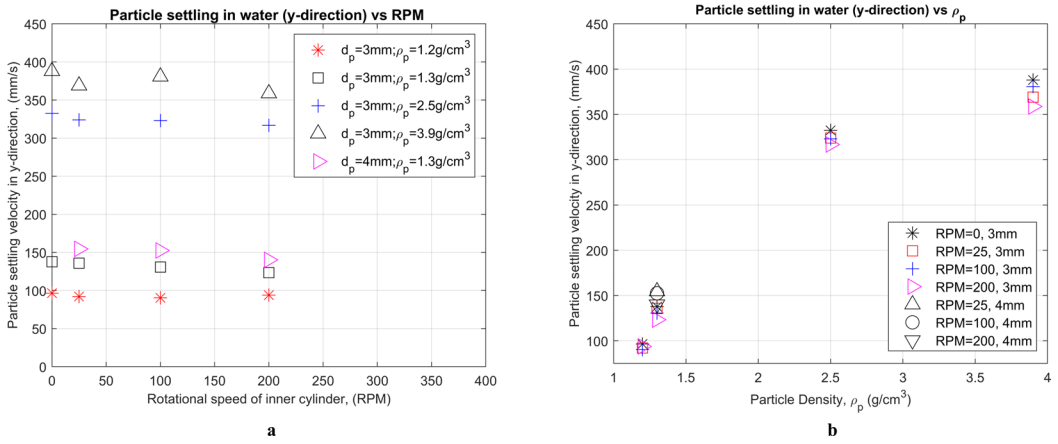

Fig. 13—Particle settling velocities in water for different (a) rotational speeds and (b) particle densities.

Downloaded from http://onepetro.org/SJ/article-pdf/doi/10.2118/219459-PA/3347625/spe-219459-pa.pdf/1 by Andres Velez on 07 February 2024

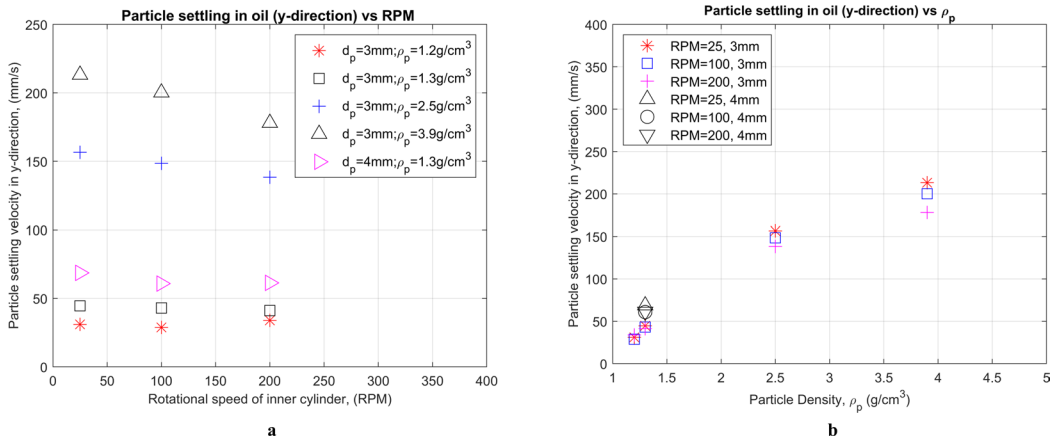

Fig. 14—Particle settling velocities in mineral oil for different (a) rotational speeds and (b) particle densities.

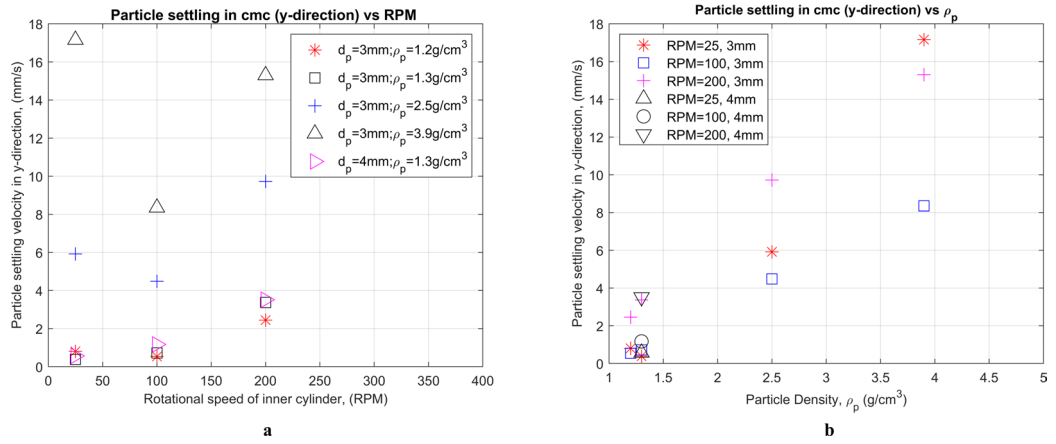

Fig. 15—Particle settling velocities in CMC 6% solution for different (a) rotational speeds and (b) particle densities.

The physical reason for these behaviors is unclear but may be due to the variations in the radial location of the particles, which may not have always been the same at the time the particles were captured by the video camera. For the CMC solution, due to low settling velocities and longer times needed to reach the video camera's field of view, the particles could have migrated radially from the initial radial position and experienced some wall effects if they came close to the surface of the stationary outer cylinder.

On the other hand, the particle settling velocity clearly increased with the particle density, as shown in **Figs. 13b, 14b, and 15b**. For water and mineral oil, **Figs. 13b and 14b** illustrate a power-law relationship between the vertical velocity and particle density, while the variation is more linear for the CMC solution **(Fig. 15b)**. Heavier particles experienced greater gravitational forces which would increase their settling velocity.

Effects of Rotational Speed and Particle Density on Horizontal Particle Velocity. The variations in the horizontal particle velocity with the rotational speed and particle density are shown in **Figs. 16 through 18** for water, mineral oil, and CMC solution, respectively. In general, the horizontal particle velocity exhibited an expected increase with the rotational speed, in accordance with the greater drag force exerted on the particle by the faster-moving fluid **(Figs. 16a, 17a, and 18a)**. On the other hand, there is a small effect of the particle density on the horizontal velocity, as indicated in **Figs. 16b and 17b**. Notably, this effect is more pronounced in water. In general, an increase in the particle density would lead to a decrease in the particle's horizontal velocity as the heavier particles would move slower under the same drag force.

Downloaded from http://onepetro.org/SJ/article-pdf/doi/10.2118/219459-PA/3347625/spe-219459-pa.pdf/1 by Andres Velez on 07 February 2024

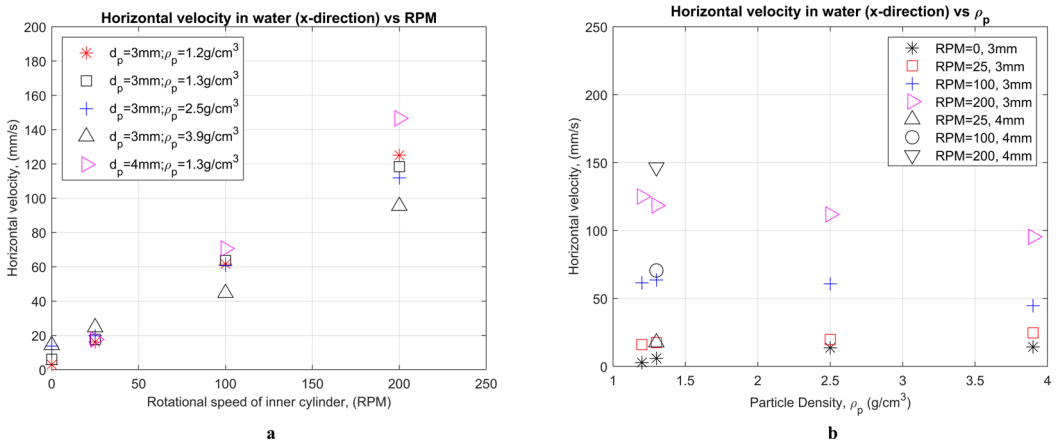

Fig. 16—Horizontal particle velocities in water for different (a) rotational speeds and (b) particle densities.

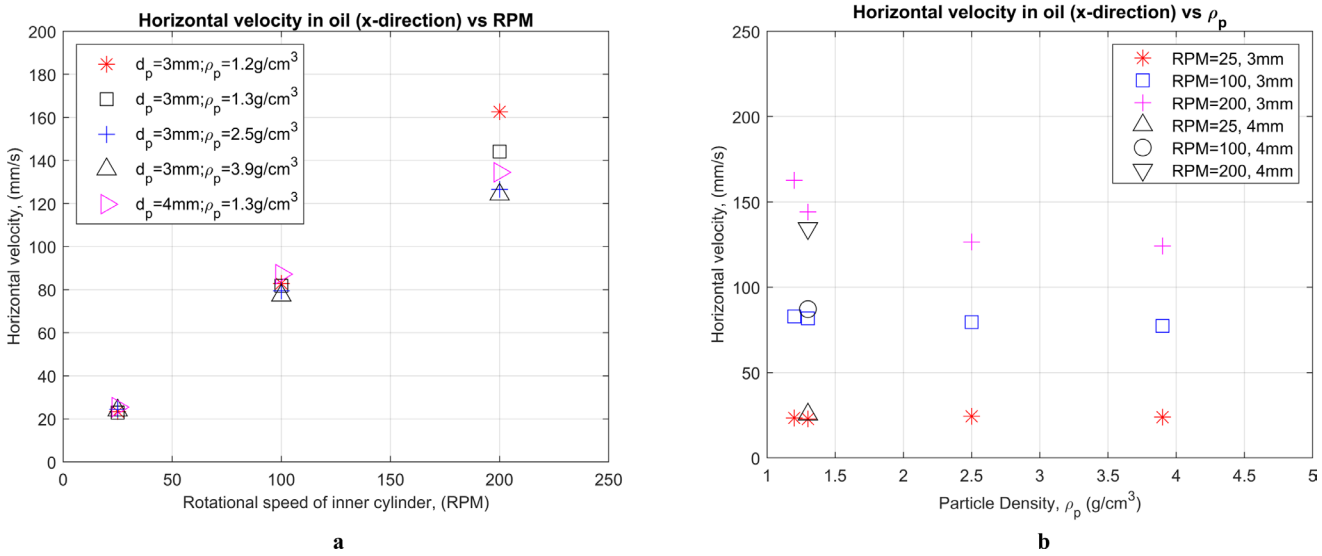

Fig. 17—Horizontal particle velocities in mineral oil for different (a) rotational speeds and (b) particle densities.

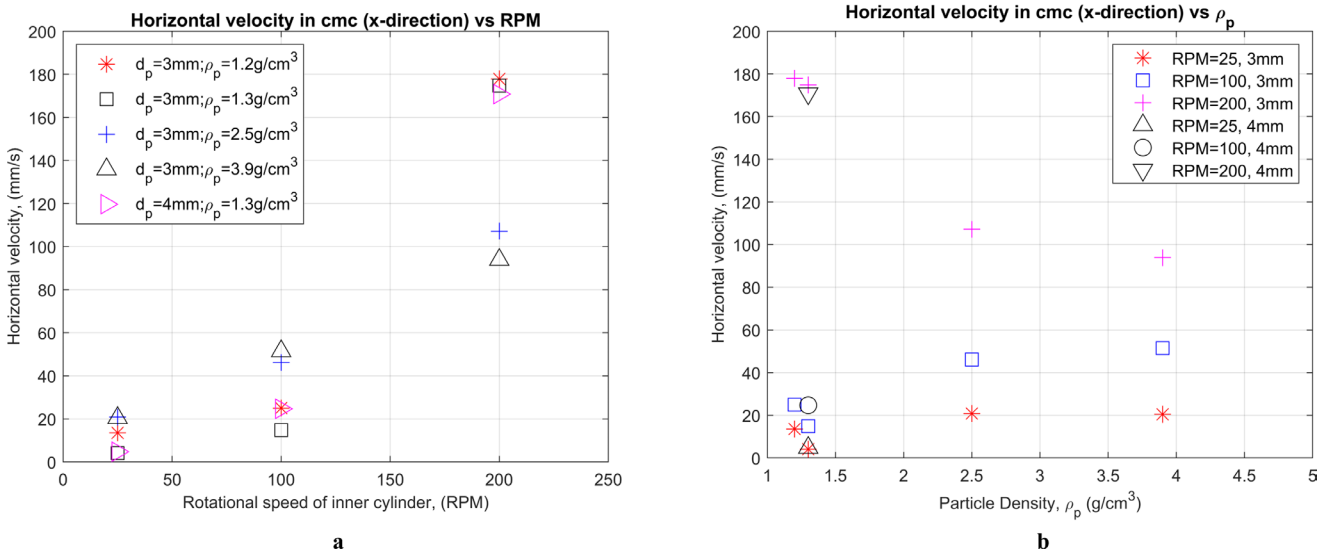

Fig. 18—Horizontal particle velocities in CMC 6% solution for different (a) rotational speeds and (b) particle densities.

Downloaded from http://onepetro.org/SJ/article-pdf/doi/10.2118/219459-PA/3347625/spe-219459-pa.pdf/1 by Andres Velez on 07 February 2024

From **Figs. 18a and 18b,** it is demonstrated that, in general, there is an increase in the horizontal velocity with an increase of rotational speed in the CMC solution as in the case of DI water and mineral oil. On the other hand, at 200 rev/min in **Fig. 18a**, heavy particles had significantly lower horizontal velocities than lighter particles, possibly due to a centrifugal force that could cause the heavy particles to migrate toward the stationary outer wall of the TC cell. Because the horizontal liquid velocity is the highest at the inner rod surface and decreases toward the surface of the stationary outer cylinder, heavy particles moving near the outer cylinder would also move more slowly than the lighter particles. Because of the slower settling speeds and longer settling times in the CMC solution compared with water and mineral oil, there was more time for the particles to migrate radially outward in the CMC solution. This was more so for heavy particles due to a centrifuge effect. These findings suggest that the high viscosity of the CMC solution substantially reduced particle motions in both horizontal and vertical directions, while centrifugal forces induced by the fluid rotation could cause heavier particles to migrate toward the outer cylinder wall, potentially influencing their horizontal and vertical velocities due to the wall effect.

Theoretical Settling Velocity. Theoretical settling velocities for various particles in DI water and mineral oil were predicted using Eq. 5 and the drag coefficient correlations, both C_{D1} and C_{D2}, for alumina, glass, PMMA, 3.0-mm CA, and 4.0-mm CA particles. For the non-Newtonian CMC solution, the terminal velocities for the particles were predicted using Eq. 32. **Fig. 19** shows the plots of instantaneous settling velocity against the vertical position for a 3-mm-diameter alumina particle with a density of 3.9 g/cm^3 in water and mineral oil. For both fluids, the settling velocities reached terminal velocity values at the location of the video camera 150 mm below the fluid surface, which is indicated by a vertical line in **Fig. 19**. The terminal velocities were found to be higher in water than in mineral oil due to the 10 times higher viscosity of mineral oil.

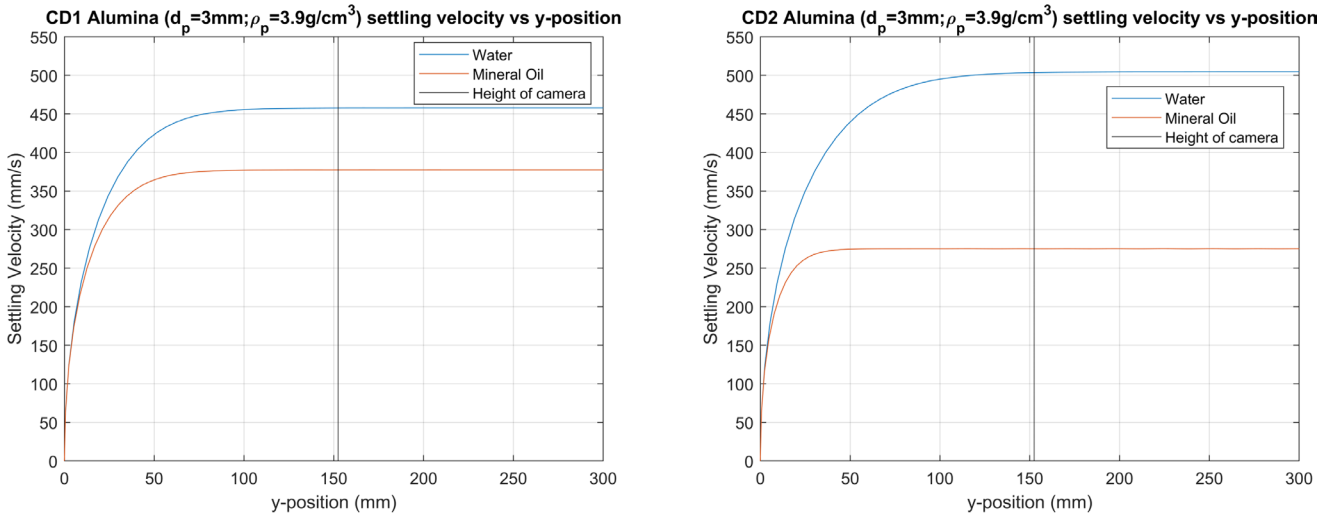

Fig. 19—Predicted settling velocity for alumina using different drag coefficients: (a) C_{D1} and (b) C_{D2}.

For the CMC solution, Eq. 32 was used with $n = 0.865$ and $K = 0.4477$ Pa·s to predict the terminal velocities for all the particles tested. The predicted terminal velocities for all three fluids and particles are listed in **Table 5.** As expected, the terminal velocities in the CMC solution were the lowest followed by mineral oil and water. Also, the drag coefficient correlation slightly affected the predicted terminal velocities for water and mineral oil.

	Water (mm/s)			Mineral Oil (mm/s)			CMC (mm/s)	
	Predicted			Predicted				
Particle	C_{D1}	C_{D2}	Experimental	C_{D1}	C_{D2}	Experimental	Predicted	Experimental
Alumina	457	503	387	377	275	213	53	17
Glass	323	343	332	246	174	157	30	6
PMMA	118	109	96	76	55	31	5.7	0.8
CA 3 mm	146	139	137	95	68	44	8.1	0.4
Ca 4 mm	172	174	155	138	97	69	12	0.6

Table 5—Predicted and experimental particle settling velocities for the three fluids in the TC cell.

Comparison of Predicted and Measured Particle Velocities. A comparison of the predicted and measured settling velocities is presented in **Table 5** and **Fig. 20**. In the case of water, the predicted results matched the experimental results for most particles, with both drag coefficient correlations, C_{D1} and C_{D2}, providing a good agreement with the experimental data. However, for the case of alumina particle with the highest density, the predicted values were higher than the measured velocities by 18% for C_{D1} and 30% for C_{D2}. For the mineral oil, the 1D particle motion equation with C_{D1} overestimated the settling velocity by about 77%, and unlike the case of water, the

Downloaded from http://onepetro.org/SJ/article-pdf/doi/10.2118/219459-PA/3347625/spe-219459-pa.pdf/1 by Andres Velez on 07 February 2024

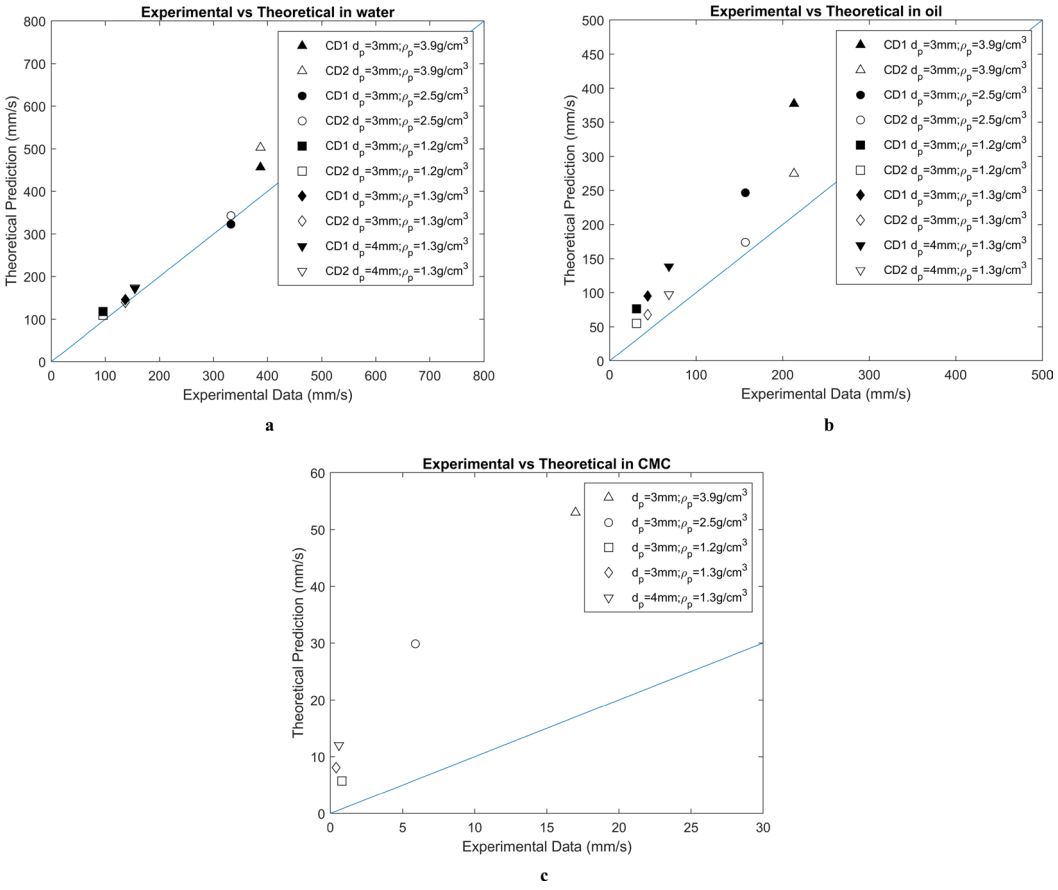

Fig. 20—Comparison of predicted and measured particle settling velocities for (a) water, (b) mineral oil, and (c) CMC 6% solution.

correlation C_{D2} yielded a better agreement, overestimating by 29%. In the case of the CMC solution, the predicted settling velocities of the alumina particle were again much higher than the measured velocities by about 200%.

As the fluid elasticity has previously been reported to affect the particle settling velocity, we examined the rheological measurement results derived from both frequency and amplitude sweeps conducted on the CMC sample. Based on these results, the CMC solution used had negligible to no elastic property; thus, the fluid elasticity was ruled out as a potential factor influencing the particle settling velocity in the present results. A possible explanation for the overpredictions of the measured particle settling velocities in the CMC solution is that the slowly settling particles tend to migrate toward the stationary outer cylinder wall due to a centrifugal force, resulting in a wall effect that would reduce the settling velocity. This radial migration of particles due to the centrifugal force is consistent with the observed formation of a filter cake on the inner wall of a wellbore during drilling operations (Mohamed et al. 2020).

Conclusions

This work was aimed at investigating the flow patterns and particle settling velocities in various fluids in a TC cell. The experiments used two Newtonian fluids (water and mineral oil) and a non-Newtonian fluid (6% CMC solution) with a shear thinning viscosity similar to oil-based DFs, which could not be used due to their opacity. It is important to note that the particles used in this work were larger in diameter and spherical in shape compared with much smaller heavy particles such as barite particles with irregular shapes contained in oil-based DFs, so the present results cannot be considered to represent barite particle sedimentation in DFs. By analyzing the data obtained from this study, the following conclusions can be drawn:

1. The flow pattern for the 6% CMC solution was found to be CCF, with no occurrence of Taylor vortices, even at the highest rotational speed (200 rev/min). Given that CMC's viscosity is only slightly higher (8%) than that of the DF at a rotational speed of 200 rev/min, Taylor vortices are not expected to occur in the actual oil-based DF.
2. The flow patterns for water were consistent with those reported in the literature: WVF at 25 rev/min and TTVF at 100 rev/min and 200 rev/min. The flow patterns observed for the mineral oil were CCF at 25 rev/min and 100 rev/min and TVF at 200 rev/min, while the CMC solution showed CCF at all rotation speeds up to 200 rev/min.
3. The PTV results indicated that the particle settling velocity was affected by the rotational speed of the inner rod for all fluids tested. As expected, the particle settling velocity decreased as the fluid viscosity increased, where the highest settling velocity for alumina particles was observed in water (350–380 mm/s), while the lowest (9–17 mm/s) was in the CMC solution.
4. The particle settling velocity increased with particle density in all three fluids as expected due to a greater gravitational force.
5. Particle horizontal velocity increased with rotational speed in all three fluids. However, it is important to mention that there was a minor effect of particle density on the horizontal velocity. In general, an increase in particle density led to a decrease in the particle's horizontal velocity.
6. The centrifugal forces generated by the fluid's rotation in the TC cell could cause heavy particles to migrate toward the stationary outer wall, and the resulting wall effect would reduce the settling velocity of heavy particles in viscous fluids. This phenomenon may be related to the formation of a layer, known as a filter cake, on the inner wall of a wellbore.

Downloaded from http://onepetro.org/SJ/article-pdf/doi/10.2118/219459-PA/3347625/spe-219459-pa.pdf/1 by Andres Velez on 07 February 2024

7. As for future research, the impact of various factors, such as particle radial migration, size distribution, concentration, wall effect, and fluid composition, can be investigated on the flow behavior of DFs. These additional insights can ultimately contribute to the development of highly efficient DFs tailored to specific geological conditions and operational requirements.

Acknowledgments

This work was supported by the National Science Foundation under the PIRE project "Multiscale, Multiphase Phenomena in Complex Fluids for the Energy Industries" (Award Number 1743794). The authors would like to thank Dr. Bjørnar Lund of SINTEF in Norway for useful discussion.

References

Ahmed, A., Basfar, S., Elkatatny, S. et al. 2022. Vermiculite for Enhancement of Barite Stability in Water-Based Mud at Elevated Temperature. *Powder Tech* **401**: 117277. https://doi.org/10.1016/j.powtec.2022.117277.

Alade, O., Mahmoud, M., and Al-Nakhli, A. 2023. Rheological Studies and Numerical Investigation of Barite Sag Potential of Drilling Fluids with Thermochemical Fluid Additive Using Computational Fluid Dynamics (CFD). *J Pet Sci Eng* **220**: 111179. https://doi.org/10.1016/j.petrol.2022.111179.

Aldea, C., Growcock, F. B., Lee, L. J. et al. 2001. Prevention of Dynamic Sag in Deepwater Invert Emulsion Fluids. Paper presented at the AADE National Drilling Conference on Drilling Technology-The Next 100 Years, Houston, Texas, USA, 27–29 March. https://www.aade.org/application/files/4415/7304/5775/AADE_51.pdf.

Al Jaberi, J., Bageri, B., Elkatatny, S. et al. 2023. Performance of Perlite as Viscosifier in Manganese Tetroxide Water Based-Drilling Fluid. *J Mol Liq* **374**: 121218. https://doi.org/10.1016/j.molliq.2023.121218.

Basfar, S., Al Jaberi, J., Elkatatny, S. et al. 2022. Prevention of Hematite Settling Using Perlite in Water-Based Drilling Fluid. *J Pet Sci Eng* **210**: 110030. https://doi.org/10.1016/j.petrol.2021.110030.

Basfar, S., Elkatatny, S., Mahmoud, M. et al. 2018. Prevention of Barite Sagging While Drilling High-Pressure High-Temperature (HPHT) Wells. Paper presented at the SPE Kingdom of Saudi Arabia Annual Technical Symposium and Exhibition, Dammam, Saudi Arabia, 23–26 April. https://doi.org/10.2118/192198-MS.

Bern, P. A., Zamora, M., Hemphill, A. T. et al. 2010. Field Monitoring of Weight-Material Sag. Paper presented at the AADE Fluids Conference and Exhibition, AADE–10, Houston, Texas, USA, 6–7 April. https://www.aade.org/application/files/3415/7261/7999/AADE-10-DF-HO-25.pdf.

Chandrasekhar, S. 1981. Hydrodynamic and Hydromagnetic Stability. In *The Stability of More General Flows Between Coaxial Cylinders*, eds. W. Marshall and D. H. Wilkinson, Vol. 8, 359–379. New York, USA: Dover Publications, Inc.

Deville, J. P. 2022. Drilling Fluids. In *Fluid Chemistry, Drilling and Completion*, Vol. 1, 115–168. Cambridge, Massachusetts, USA: Gulf Professional Publishing/Elsevier.

Dracos, T. 1996. *Three-Dimensional Velocity and Vorticity Measuring and Image Analysis Techniques*, 155. Zürich: Kluwer Academic Publishers.

Elkatatny, S. 2018. Enhancing the Stability of Invert Emulsion Drilling Fluid for Drilling in High-Pressure High-Temperature Conditions. *Energies* **11** (9): 2393. https://doi.org/10.3390/en11092393.

Fadl, A. M., Abdou, M. I., El-Sayed Ahmed, H. et al. 2020. Delaminated Iron Ore (Hematite-Barite) as Alternative Weighting Agent to Barite in Petroleum Drilling Fluids Engineering Operations and Mechanism Study. *Ain Shams Eng J* **11** (4): 1317–1337. https://doi.org/10.1016/j.asej.2020.03.005.

Fakour, M., Rahbari, A., Moghadasi, H. et al. 2018. Analytical Study of Unsteady Sedimentation Analysis of Spherical Particle in Newtonian Fluid Media. *Therm Sci* **22** (2): 847–855. https://doi.org/10.2298/TSCI160602181F.

Ferreira, J. M., Duarte Naia, M., and Chhabra, R. P. 1998. An Analytical Study of the Transient Motion of a Dense Rigid Sphere in an Incompressible Newtonian Fluid. *Chem Eng Commun* **168** (1): 45–58. https://doi.org/10.1080/00986449808912706.

Growcock, F. and Harvey, T. 2005. Drilling Fluids. In *Drilling Fluids Processing Handbook*, Vol. 2, 15–68. Burlington, Massachusetts, USA: Gulf Professional Publishing/Elsevier. https://doi.org/10.1016/B978-075067775-2/50003-2.

Islam, M. R. and Hossain, M. E. 2021. *Drilling Engineering: Towards Achieving Total Sustainability*. Cambridge, Massachusetts: Gulf Professional Publishing/Elsevier.

Jalaal, M., Ganji, D. D., and Ahmadi, G. 2010. Analytical Investigation on Acceleration Motion of a Vertically Falling Spherical Particle in Incompressible Newtonian Media. *Adv Powder Technol* **21** (3): 298–304. https://doi.org/10.1016/j.apt.2009.12.010.

Kalman, H. and Matana, E. 2022. Terminal Velocity and Drag Coefficient for Spherical Particles. *Powder Technol* **396**: 181–190. https://doi.org/10.1016/j.powtec.2021.10.053.

Kalman, H. and Portnikov, D. 2023. New Model to Predict the Velocity and Acceleration of Accelerating Spherical Particles. *Powder Technol* **415**: 118197. https://doi.org/10.1016/j.powtec.2022.118197.

Malhotra, S. and Sharma, M. M. 2012. Settling of Spherical Particles in Unbounded and Confined Surfactant-Based Shear Thinning Viscoelastic Fluids: An Experimental Study. *Chem Eng Sci* **84**: 646–655. https://doi.org/10.1016/j.ces.2012.09.010.

Malvandi, A., Moshizi, S. A., and Ganji, D. D. 2014. An Analytical Study on Unsteady Motion of Vertically Falling Spherical Particles in Quiescent Power-Law Shear-Thinning Fluids. *J Mol Liq* **193**: 166–173. https://doi.org/10.1016/j.molliq.2013.12.042.

Maxey, J. 2007. Rheological Analysis of Static and Dynamic Sag in Drilling Fluids. *Ann Trans Nordic Rheol Soc* 15: 181–188. https://nrs.blob.core.windows.net/pdfs/nrspdf-f3741626-0a14-4902-8c2a-aaa94c73eb68.pdf.

Mohamed, A., Elkatatny, S., and Al-Majed, A. 2020. Removal of Calcium Carbonate Water-Based Filter Cake Using a Green Biodegradable Acid. *Sustainability* **12** (3): 994. https://doi.org/10.3390/su12030994.

Nasab, S. H. 2017. *Free Falling of Spheres in a Quiescent Fluid*. MSc Thesis, Concordia University, Montréal, Québec. https://core.ac.uk/download/pdf/211520071.pdf.

Nguyen, T. C., Miska, S., Saasen, A. et al. 2014. Using Taguchi and ANOVA Methods to Study the Combined Effects of Drilling Parameters on Dynamic Barite Sag. *J Pet Sci Eng* **121**: 126–133. https://doi.org/10.1016/j.petrol.2014.06.029.

Nguyen, T., Miska, S., Yu, M. et al. 2009. Combined Effects of Eccentricity and Pipe Rotation on Dynamic Barite Sag-Analysis of Different Impacts on Pipe Rotation in a Flow Loop and Rotation in a Modified Rotational Viscometer on Barite Sag. Paper presented at the AADE National Technical Conference and Exhibition, New Orleans, Louisiana, USA. AADE 2009NTCE-12-01. https://www.aade.org/download_file/2579/489.

Nguyen, T., Miska, S., Yu, M. et al. 2011. Experimental Study of Dynamic Barite Sag in Oil-Based Drilling Fluids Using a Modified Rotational Viscometer and a Flow Loop. *J Pet Sci Eng* **78** (1): 160–165. https://doi.org/10.1016/j.petrol.2011.04.018.

Ofei, T. N., Kalaga, D. V., Lund, B. et al. 2021. Laboratory Evaluation of Static and Dynamic Sag in Oil-Based Drilling Fluids. *SPE J.* **26** (03): 1072–1091. https://doi.org/10.2118/199567-PA.

Okensaya, T., Abdukarimov, A., and Kuru, E. 2020. Generalized Models for Predicting the Drag Coefficient and Setlling Velocity of Rigid Spheres in Viscoelastic and Viscoinelastic Power-Law Fluids. *J Pet Sci Eng* **191**. https://doi.org/10.1016/j.petrol.2020.107077.

Downloaded from http://onepetro.org/SJ/article-pdf/doi/10.2118/219459-PA/3347625/spe-219459-pa.pdf/1 by Andres Velez on 07 February 2024

Omland, T. H., Saasen, A. and Amundsen, P. A. 2007. Detection Techniques Determining Weighting Material Sag in Drilling Fluid and Relationship to Rheology. *Ann Trans Nordic Rheol Soc* 15: 1–9. https://nrs.blob.core.windows.net/pdfs/nrspdf-a5b9f18e-7a1e-46dc-adca-75a4a27ef91b.pdf.

Polezhaev, Y. V. and Chircov, I. V. 2011. *Drag Coefficient*. https://doi.org/10.1615/AtoZ.d.drag_coefficient (accessed 2 February 2022).

Schiller, L. and Naumann, Z. 1935. A Drag Coefficient Correlation. *Zeitschrift des Vereines Deutscher Ingenieure* 77: 318-320.

Shah, S. N., El Fadili, Y., and Chhabra, R. P. 2007. New Model for Single Spherical Particle Settling Velocity in Power Law (Visco-Inelastic) Fluids. *Int J Multiph Flow* **33** (1): 51–66. https://doi.org/10.1016/j.ijmultiphaseflow.2006.06.006.

Song, X., Xu, Z., Li, G. et al. 2017. A New Model for Predicting Drag Coefficient and Settling Velocity of Spherical and Non-Spherical Particle in Newtonian Fluid. *Powder Tech* **321**: 242–250. https://doi.org/10.1016/j.powtec.2017.08.017.

Torabi, M. and Yaghoobi, H. 2011. Novel Solution for Acceleration Motion of a Vertically Falling Spherical Particle by HPM–Padé Approximant. *Adv Powder Technol* **22** (5): 674–677. https://doi.org/10.1016/j.apt.2011.02.013.

White, F. M. 2016. *Fluid Mechanics*, Chap. 4, 266–269. New York City: McGraw-Hill Education.

Yoshida, K., Tasaka, Y., Murai, Y. et al. 2009. Mode Transition in Bubbly Taylor-Couette Flow Measured by PTV. *J. Phys.: Conf. Ser* **147**: 012013. https://doi.org/10.1088/1742-6596/147/1/012013.

Zamora, M. 2011. Taming of the Shoe. Paper presented at the AADE National Technical Conference and Exhibition, AADE–11, Houston, Texas, USA, 12–15 April. https://www.aade.org/application/files/8115/7261/8788/AADE-11-NTCE-44.pdf.

Zhu, Z.-P., Song, X.-Z., Kuru, E. et al. 2022a. Settling Behavior of Spherical Particles in Eccentric Annulus Filled with Viscous Inelastic Fluid. *Pet Sci* **19** (4): 1653–1663. https://doi.org/10.1016/j.petsci.2022.04.003.

Zhu, Z., Zhou, M., Song, X. et al. 2022b. Settling Behavior of Spherical Particles in Vertical Annulus: Experimental Study and Model Development. *Particuology* **68**: 114–123. https://doi.org/10.1016/j.partic.2021.11.005.

Downloaded from http://onepetro.org/SJ/article-pdf/doi/10.2118/219459-PA/3347625/spe-219459-pa.pdf/1 by Andres Velez on 07 February 2024